

Trans-stenotic pressure gradient estimation using a modified Bernoulli equation

Ali Amiri^{1,2}, Johan T. Padding¹, Selene Pirola^{2,*}, and Willian Hogendoorn^{1,*}

¹Delft University of Technology, Complex Fluid Processing (Process & Energy), Delft, 2628 CB, The Netherlands

²Delft University of Technology, Cardiovascular Biomechanics (BioMechanical Engineering), Delft, 2628 CD, The Netherlands

*S.Pirola@tudelft.nl (Selene Pirola), W.J.Hogendoorn@tudelft.nl (Willian Hogendoorn)

*Senior authors contributed equally to this work

ABSTRACT

Accurate non-invasive estimation of trans-stenotic pressure gradients remains a challenge. In clinical practice, pressure gradients are often estimated from velocity measurements using Bernoulli-based formulas, but these simplified relations do not explicitly account for how pressure losses change with the flow regime. Here, we introduce a modified Bernoulli (MB) formulation that incorporates regime-dependent pressure losses through a Reynolds-number-dependent loss coefficient. Steady in-vitro experiments were performed in an idealized stenosis model over physiologically relevant flow rates (0.65 – 3.9 L/min), combining direct pressure measurements with ultrasound imaging velocimetry (UIV) and phase-contrast magnetic resonance imaging (PC-MRI) to measure velocities. The MB model was calibrated from the measured pressure drops and then evaluated against the simplified Bernoulli (SB) and extended Bernoulli (EB) formulations. Over the tested flow regime, MB agreed best with the measurements (typically within about $\pm 10\%$). SB and EB showed larger biases, with errors of roughly 10 – 55% (SB) and -15 – 25% (EB), and overestimated the pressure drop in the clinically relevant range. We additionally quantified the effect of PC-MRI in-plane pixel size on MRI-based pressure estimates. Coarse sampling of the stenosis throat (only 3 – 4 pixels across the throat radius) led to systematic underestimation of flow rate and bulk velocity (about -34 to -44%) and, consequently, of the MB-predicted pressure drop (about -52 to -62%). In contrast, the peak throat velocity was substantially less sensitive to pixel size, resulting in smaller estimation errors (about -13 to -18.7%) when used as input for the MB. Overall, the results demonstrate that accounting for flow-regime-dependent loss mechanisms enhances pressure drop estimation, and that sufficient sampling of the stenotic throat is crucial for MRI-based flow rate and pressure drop estimation. In addition, peak-velocity-based MB pressure drop estimations are less sensitive to pixel size.

Introduction

Over the past few decades, cardiovascular diseases have become one of the top three causes of death around the world, with arterial stenosis ranking among the most significant contributors to global cardiovascular disease¹. Stenosis is a common disease, affecting up to 5% of heart valves² and 10% of blood vessels³. It leads to pathological pressure-drops, which increase the heart workload and cause cardiovascular complications and mortality⁴. Therefore, pressure gradients serve as crucial indicators of stenosis severity.

One of the major challenges in the management of stenosis is the accurate assessment of lesion severity⁵. The hemodynamic significance could be assessed by measuring the pressure drop across the narrowed region. However, accurate determination of trans-stenotic pressure gradients represents a critical challenge in cardiovascular medicine, directly influencing therapeutic decisions for patients with arterial stenoses and valvular disease. While catheter-based measurements remain the clinical gold standard, their invasive nature and associated risks have motivated extensive research into non-invasive alternatives^{6,7}. The convergence of advanced medical imaging, computational methods, and refined analytical methods has created new possibilities for pressure gradient assessment. However, significant challenges persist in translating these approaches to routine clinical practice.

4D-flow MRI (time-resolved 3D phase-contrast magnetic resonance imaging) has become a key technique for non-invasive quantification of cardiovascular hemodynamics, providing volumetric velocity fields that are increasingly used to characterize stenotic jets, secondary flow structures, and clinically relevant flow-derived biomarkers^{8–10}. Markl et al. outline both the clinical potential and the practical limitations of 4D-flow MRI for cardiovascular assessment⁸. Multiple studies emphasize that quantitative interpretation is strongly limited by acquisition constraints, most notably pixel size^{6,11,12}. Larger pixel sizes can systematically bias measured velocities through partial-volume effects (PVE). This bias is amplified by smoothing of

sharp gradients, particularly in narrow stenotic throats and high-shear regions. Collectively, this literature motivates explicitly accounting for MRI in-plane pixel size when using phase-contrast (PC)-MRI data as input to pressure drop estimation, because pressure losses scale strongly with characteristic velocities.

Simplified formulations of the Bernoulli equation have long dominated clinical practice for non-invasive pressure-drop estimation, such as echocardiographic evaluation of valvular stenosis¹³. The simplified Bernoulli equation (SB) remains widely used, even though its limitations are well documented^{6,14–18}. Kazemi et al.¹⁵ evaluated relative pressure estimation in a stenotic phantom using 4D-flow MRI. They found that the pressure drop estimation from SB could deviate by 22% at moderate flow and 40% at the highest flow rate tested. Garcia et al.¹⁹ advanced this model by introducing an extended Bernoulli equation (EB). In this model the ratio between the effective orifice area and the vessel area is incorporated. This effectively accounts for the downstream pressure recovery due to the jet deceleration. However, despite this improvement, the EB does not explicitly capture the change in flow physics from laminar, viscous-dominated losses to turbulent, inertia-dominated losses²⁰.

Turbulent losses and pressure recovery are not fully accounted for in the SB and EB models. Quantification of turbulence has emerged as a promising avenue to improve the estimation of trans-stenotic pressure gradient. Ha et al.⁶ demonstrated that turbulence production defined using 4D-flow MRI correlates strongly with irreversible pressure-losses across stenoses. Similarly, Casas et al.²¹ showed that quantification of turbulent kinetic energy (TKE) can provide geometry-dependent estimates of net trans-stenotic pressure gradients, with more severe stenoses exhibiting higher turbulent energy dissipation. This finding further supports the necessity to account for turbulent energy dissipation for an accurate estimation of lesion severity²², especially during exercise or pharmacologic stress.

This link to turbulent energy dissipation highlights that the pressure-loss coefficient depends on the flow regime, which is typically characterized by the Reynolds number (Re). However, many clinically established estimation methods still assume a constant flow regime with independent correlations. This flow regime sensitivity has profound clinical implications, particularly for quantifying stenosis severity. To illustrate: a stenosis assessed as moderate at rest may behave quite differently during exercise when flow rates increase and the flow becomes turbulent^{23–25}. Several studies have used analytical solutions for flow through constricted geometries to incorporate flow regime effects into the model^{26–29}. Young and Tsai²⁶ indicated that pressure-loss mechanisms vary significantly across laminar, transitional, and turbulent regimes. For steady flow they showed that the pressure gradient can be written as the sum of a viscous term and a turbulence dissipation term. This approach was later extended to account for the effects of pulsatile flow²⁸ and stenosis shape³⁰. However, their correlation, expressed solely in terms of Re , cannot be directly applied in routine clinical settings particularly with Doppler echocardiography and PC-MRI, which primarily provide peak velocity and flow rate. A recent study derived the SB expression in terms of flow rate for cerebral venous flow and reported good agreement with CFD³¹. This indicates that deriving an SB model in terms of flow rate can work in their specific application. However, this approach does not account for turbulence-related losses, which is acceptable in cerebral venous flow where can likely be ignored.

In summary, despite recent advances, significant gaps remain in existing models due to their lack of turbulent energy dissipation and pressure recovery contributions. In addition, when the velocity in the model is obtained using MRI, the model accuracy depends strongly on in-plane pixel size, which is addressed in the second part of the present study. This study aims to address these gaps by investigating trans-stenotic pressure gradients in an idealized stenosis model, using ultrasound imaging velocimetry (UIV) and PC-MRI coupled with direct pressure measurements. By examining a range of Re numbers spanning laminar and turbulent regimes, we aim to: (1) establish the relationship between peak and bulk velocities in the stenosis throat, the associated Re -dependent loss mechanisms, and pressure drop, and (2) integrate MRI-based velocities into this framework to quantify how a pixel-size-dependent velocity bias affects the trans-stenotic pressure gradient predictions.

Methods

Bernoulli Methods for pressure gradient Estimation

Simplified Bernoulli Equation

The SB equation represents the most clinically prevalent method for pressure estimation⁶. This method is derived from the Navier-Stokes equation under several simplifying assumptions: inviscid flow, negligible body forces, steady flow conditions, and negligible upstream velocity. Under these assumptions, the pressure difference is given by:

$$\Delta p_{SB} = p_1 - p_2 \approx \frac{1}{2} \rho V_{\text{peak,t}}^2 \quad (1)$$

where p_1 and p_2 are the upstream and downstream pressures respectively, and $V_{\text{peak,t}}$ is the peak velocity at the stenosis. In clinical applications, especially echocardiography, the pressure gradient in mmHg is reported as⁷:

$$\Delta p_{SB} = p_1 - p_2 \approx 4V_{\text{peak,t}}^2 \quad (2)$$

assuming a constant blood density $\rho_b = 1060 \text{ kg/m}^3$ and using $1 \text{ mmHg} = 133.322 \text{ Pa}$ for unit conversion.

The pressure-loss coefficient for the SB method is defined as the ratio of the measured pressure drop and the dynamic pressure:

$$K_{\text{SB}} = \frac{\Delta p_{\text{SB}}}{\frac{1}{2}\rho V_{\text{bulk}}^2} = \frac{V_{\text{peak,t}}^2}{V_{\text{bulk}}^2} \quad (3)$$

where V_{bulk} is the bulk velocity in the upstream vessel. This dimensionless pressure-loss coefficient enables comparison for different geometries and operating conditions.

Extended Bernoulli Equation

The EB equation accounts for the geometric properties of the stenosis through the effective orifice area and the anatomical cross-sectional area, resulting in an area-ratio correction that captures potential downstream pressure recovery¹⁹.

$$\Delta p_{\text{EB}} = p_1 - p_2 \approx \frac{1}{2}\rho V_{\text{peak,t}}^2 \left(1 - \frac{A_t}{A_A}\right)^2 = \Delta p_{\text{SB}} \left(1 - \frac{A_t}{A_A}\right)^2 \quad (4)$$

where A_t is the effective orifice area, and A_A is the upstream anatomical cross-sectional area of the vessel. The correction factor $\left(1 - \frac{A_t}{A_A}\right)^2$ accounts for the geometric contraction and provides a more accurate representation of the pressure-velocity relationship in stenotic flows compared to the SB approach.

The pressure-loss coefficient for the EB method can be calculated as:

$$K_{\text{EB}} = \frac{\Delta p_{\text{EB}}}{\frac{1}{2}\rho V_{\text{bulk}}^2} = \frac{V_{\text{peak,t}}^2}{V_{\text{bulk}}^2} \left(1 - \frac{A_t}{A_A}\right)^2 \quad (5)$$

where Δp_{EB} represents the pressure drop from the EB approach.

Modified Bernoulli Equation

For steady flow, the pressure gradient from the modified Bernoulli (MB) equation can be written as the sum of a viscous term and a turbulent term²⁶:

$$\Delta p_{\text{MB}} = \frac{1}{2}\rho V_{\text{bulk}}^2 \left(\frac{k_v}{Re} + k_t \left(1 - \frac{A_A}{A_t}\right)^2 \right) = \frac{1}{2}\rho V_{\text{bulk}}^2 K_{\text{MB}} \quad (6)$$

where the first term represents viscous losses, the constant k_v is a geometry-dependent coefficient and Re is the Reynolds number $Re = \frac{\rho V_{\text{bulk}} D}{\mu} = \frac{4\rho Q}{\pi\mu D}$, where D is the inlet pipe diameter, μ is the dynamic viscosity, and Q is the volumetric flow rate. The second term reflects losses due to turbulence, and the coefficient k_t is the expansion loss coefficient. The corresponding pressure-loss coefficient is defined as:

$$K_{\text{MB}} = \frac{\Delta p_{\text{MB}}}{\frac{1}{2}\rho V_{\text{bulk}}^2} = \frac{k_v}{Re} + k_t \left(1 - \frac{A_A}{A_t}\right)^2 \quad (7)$$

In this study, the coefficients k_t and k_v were obtained by fitting Eq. (7) to the measured pressure gradient data Δp_{EXP} . The bulk velocity V_{bulk} was determined via UIV measurements upstream of the idealized model. The values obtained were $k_v = 62.4 \times 10^3$ and $k_t = 1.41$. This Re -dependent pressure-loss coefficient captured the transition from high loss coefficients at low Re to an asymptotic value at high Re . Using the definition of Re , we defined the K_{MB} in terms of flow rate through the relation:

$$K_{\text{MB}} = \frac{k_v \pi \mu D}{4\rho Q} + k_t \left(1 - \frac{A_A}{A_t}\right)^2 = \frac{k'_v}{Q} + k_t \left(1 - \frac{A_A}{A_t}\right)^2 \quad (8)$$

with $k'_v = \frac{k_v \pi \mu D}{4\rho}$. Also, by defining C as the velocity ratio at the throat, $C = V_{\text{peak,t}}/V_{\text{bulk,t}}$, where $V_{\text{bulk,t}}$ is the bulk velocity in the throat, the pressure-loss coefficient using the MB can be defined based on $V_{\text{peak,t}}$:

$$K_{\text{MB}} = C \frac{k'_v}{A_t V_{\text{peak,t}}} + k_t \left(1 - \frac{A_A}{A_t}\right)^2 = \frac{k''_v}{V_{\text{peak,t}}} + k_t \left(1 - \frac{A_A}{A_t}\right)^2 \quad (9)$$

where $k''_v = C \frac{k'_v}{A_t} = C \frac{k_v \pi \mu D}{4\rho A_t}$. Using the SB formulation of the pressure drop (Eq. 1), the pressure drop obtained using the MB equation becomes:

$$\Delta p_{MB} = \frac{1}{2}\rho \left(\frac{Q}{A_A}\right)^2 K_{MB} = \frac{1}{2}\rho \left(\frac{V_{\text{bulk,t}}A_t}{A_A}\right)^2 K_{MB} = \Delta p_{SB} \left(\frac{A_t}{A_A}\right)^2 \frac{K_{MB}}{C^2} \quad (10)$$

Importantly, K_{MB} in this expression is not a constant but depends on $V_{\text{peak,t}}$ as shown in Eq. 9.

In-vitro experimental facility

The experiments are performed in a closed-loop facility, shown in Figure 1a. The flow is driven by a centrifugal pump (compactON 2100, EHEIM GmbH, Deizisau, Germany) that recirculates water from a reservoir. The flow rate was adjusted with a manual valve that is installed after the pump. The flowrate and water temperature were monitored using an electromagnetic in-line flowmeter (AF-E 400, KROHNE, Duisburg, Germany), that is located after the valve. Subsequently, there is a 6 m straight polymethyl methacrylate (PMMA) pipe with inner diameter $D = 20$ mm and the Food and Drug Administration (FDA) nozzle geometry. A flexible hose closes the flow loop, connecting the PMMA pipe to the reservoir. During the experiments the water is kept at a temperature of approximately $T = 22^\circ\text{C}$ to ensure constant fluid properties ($\rho \approx 998 \text{ kg/m}^3$, $\mu \approx 1.0 \times 10^{-3} \text{ Pa}\cdot\text{s}$). Pressure measurements were obtained using Validyne DP15 variable reluctance pressure sensor (Validyne Engineering Corporation, Northridge, CA, USA), which were placed at two locations P_1 and P_2 to capture pressure variations across the test section (Fig. 1a). Data were acquired using a National Instruments DAQ (Austin, TX, USA), recorded at 1000 Hz for 10 s for each measurement. The experimental flow rates, corresponding Re number, and bulk and peak velocities obtained from the UIV analysis are reported in Supplementary Table S1.

The experimental model was a transparent FDA benchmark nozzle milled from polymethyl methacrylate (PMMA; Perspex), and is shown in Fig. 1b. The geometry was scaled-up by a factor of three with respect to the reference geometry³². This results in an overall length of $L = 104.5$ mm, inlet and outlet diameters $D = 20$ mm, and a conical convergence with a 10° half-angle resulting in a throat diameter of $D_t = 6.6$ mm and throat length of $L_z = 40$ mm. To provide a fully developed inlet condition, the nozzle inlet was positioned 130 pipe diameters (130D) downstream of the flowmeter, resulting stable, reproducible velocity profiles at the measurement location. This geometry represents a canonical case for an idealized stenosis model³².

UIV acquisition and processing

Images were acquired with a Verasonics Vantage research ultrasound system (Verasonics Inc., Kirkland, WA, USA). The system is coupled to a linear array transducer (L11-5v) of 128 elements with a pitch of 0.3 mm and an elevation focus at 18 mm. The probe was operated at a center frequency of 7.5 MHz (bandwidth 6.5-8.5 MHz) and provided a lateral field of view of $L_z = 38.4$ mm along the array and a depth of 30 mm. Image acquisition was performed using parallel beamforming, with all array elements transmitting and receiving simultaneously. The measurement geometry and axes are shown in Fig. 1c: the imaging depth y was measured downward from the transducer surface into the flow. To improve the signal-to-noise (SNR) ratio of the ultrasound images, the PMMA wall thickness at the location of the throat was reduced from 16.7 mm to 4.4 mm³³⁻³⁵. The space between the flat surface created after removing the wall and the transducer was filled with water to provide acoustic coupling. The flow was seeded with Vestosint particles (Degussa-Hüls, Frankfurt, Germany) with a mean diameter $d_p = 56 \mu\text{m}$ and density $\rho_p = 1016 \text{ g/cm}^3$.

The acquisition rate was varied from 600 to 1600 Hz, dependent on the flow velocity. For each flow condition, 2000 frames were recorded, resulting in 1000 image pairs for correlation. The grayscale image in Fig. 1d (left) shows the B-mode images, while the right image shows the background subtracted B-mode image; red arrows indicate the local velocity vectors. Velocity fields were then obtained using a modified version of PIVware MATLAB script³⁶. We perform two-pass processing without any advanced techniques such as window offsets or iterative image deformation^{37,38}. Interrogation windows of [16 64] pixels followed by [8 32] pixels were used, each with 50% overlap. Correlation averaging was applied by averaging the cross-correlation maps over the full set of image pairs before estimating the final velocity vectors.

Prior to the pressure drop analysis, the accuracy of the UIV measurements was validated through comparison with theoretical bulk velocity calculations. Velocity measurements were conducted upstream of the idealized stenosis model in the straight pipe section and in the throat section for flow rates ranging from 1 to 4 L/min. The bulk velocity from UIV measurements V_{bulk} was calculated using radial integration, assuming a symmetric profile which was confirmed by the velocity profile:

$$V_{\text{bulk}} = \frac{2}{R^2} \int_0^R u(r) \cdot r dr \quad (11)$$

where $u(r)$ represented the measured velocity profile as a function of radial position r according to Fig. 1a.

MRI acquisition and processing

MRI measurements were obtained with a 3 T preclinical system (MR Solutions, UK); using a 2D gradient-echo phase-contrast sequence³⁹. Symmetric velocity encoding was used, in which equal and opposite encodes ($+V_{\text{enc}}$ and $-V_{\text{enc}}$) were acquired

and differenced, rather than using a separate flow-compensated reference. Further sequence-design details are provided in the Supplementary Material. The MRI signals were acquired using a quadrature receiver coil with a diameter of 54 mm. The center of a single slice (thickness 5 mm) was positioned at the minimum cross-section at $z = -0.036$ m with $z = 0$ at the beginning of the expansion (Fig. 1f). Although we report in-plane pixel size, velocities are voxel-averaged because the slice thickness is 5 mm. For each flow rate in the range 1.5 to 3.5 L/min, one dataset was acquired at an in-plane pixel size of 0.13 mm/px, and the coarser pixel sizes (0.25, 0.50, 1.00, and 1.33 mm/px) were generated retrospectively during reconstruction; further details are provided in the Supplementary Material. MRI bulk velocities V_{bulk} were obtained by integrating over the segmented lumen, compared to bulk velocity from the flowmeter, and the relative error was computed for every flow-rate–pixel-size pair. Table 1 shows the parameters that were used for the MRI acquisitions and the reconstruction matrix sizes.

| Parameter | Value |
|---|--|
| Acquired matrix size (read \times phase \times slice) | $256 \times 256 \times 1$ |
| Reconstructed matrix sizes (read \times phase \times slice) | $128 \times 128 \times 1$ $64 \times 64 \times 1$ $32 \times 32 \times 1$ $24 \times 24 \times 1$ |
| Field of view (FOV) | $32 \times 32 \text{ mm}^2$ |
| Slice thickness | 5 mm |
| Repetition time (TR) | 50 ms |
| Echo time (TE) | 3 ms |
| RF flip angle (α) | 10° |
| Velocity encoding (V_{enc}) | 110-300 cm/s |
| Number of averages | 10 |

Table 1. MRI parameters used.

Calibrating and applying the MB model

Figure 1 summarizes the experimental and analytical workflow used to define the MB model. Pressure drops across the idealized stenosis model were measured between pressure taps P_1 and P_2 for Re corresponding to flow rates of 0.65 – 3.9 L/min (Fig. 1a), and time-averaged to obtain the experimental pressure loss coefficient and calibrate K_{MB} (Eq. (9)), yielding k_v'' (or k_v') and k_t . Peak velocities, the throat velocity ratio, and flow rate were then measured with UIV and PC-MRI and used as inputs to the SB, EB, and MB formulations for $Q = 0.85 – 3.5$ L/min (Figs. 1c-f), enabling comparison of model predictions against the measurements (Fig. 1g). The error analysis for the pressure-loss coefficient, pressure drop, and bulk velocity was based on the percentage error, root-mean-square error (RMSE), and mean absolute percentage error (MAPE), defined as follows:

$$\text{Percentage Error} = \frac{K_{\text{MODEL},i} - K_{\text{EXP},i}}{K_{\text{EXP},i}} \times 100 \quad (12)$$

$$\text{RMSE} = \sqrt{\frac{1}{N} \sum_{i=1}^N (K_{\text{MODEL},i} - K_{\text{EXP},i})^2} \quad (13)$$

$$\text{MAPE} = 100 \times \frac{1}{N} \sum_{i=1}^N \left| \frac{K_{\text{MODEL},i} - K_{\text{EXP},i}}{K_{\text{EXP},i}} \right| \quad (14)$$

where i indexes the measurement cases (e.g., each flow rate condition) and N is the total number of cases included in the error calculation.

Results

Pressure-loss coefficient

The pressure-loss coefficient over the stenotic geometry as function of Re is shown in Fig. 2a. The experimental values (EXP, black triangles) show a significant dependence on Re , decreasing from roughly 180 at $Re = 1000$ to about 107 at $Re = 4000$. Additionally, the predicted pressure-loss coefficient by the different models (MB, SB, and EB) are added. A fitted empirical correlation (FIT, solid black line) based on the Young relation^{26,28} reproduces this trend well, showing higher losses at low Re and approaching an asymptotic value as Re increases. The UIV-derived parameters $V_{\text{peak,t}}$ and C were measured for six

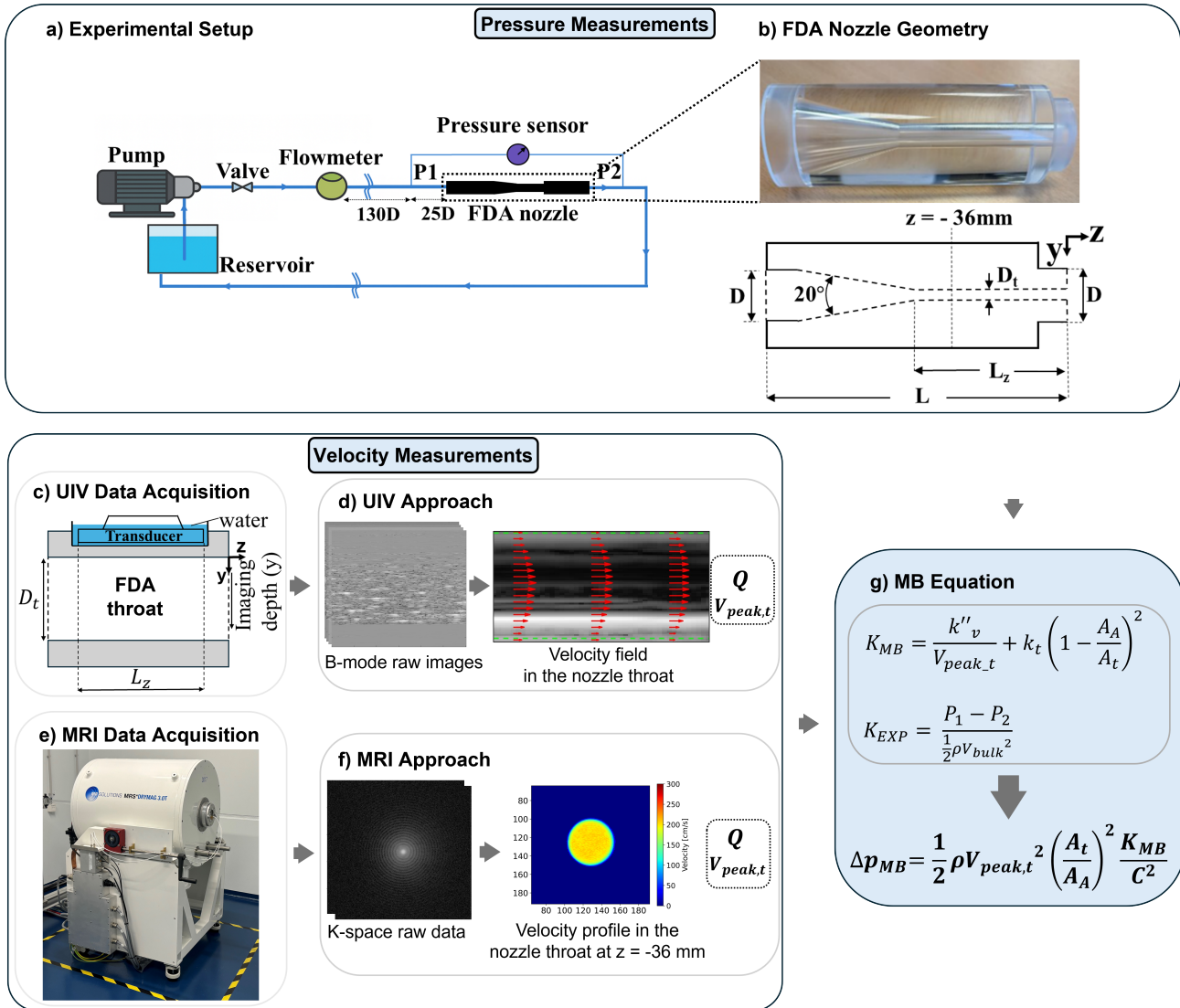


Figure 1. Overview of experimental approach and methodology: (a) closed-loop flow rig; (b) the FDA nozzle geometry and dimensions; (c) ultrasound imaging configuration at the nozzle throat; (d) UIV approach; (e) image of the MRI system and part of the experimental facility; (f) MRI approach; (g) MB formulation, where the pressure-loss coefficient K_{MB} is calibrated using the experimental coefficient K_{EXP} .

flow rates and listed in Supplementary Table S1. For the MB model (Eq. 9), $V_{peak,t}$ and C were used as inputs. The results from the SB and EB models were obtained using only $V_{peak,t}$ as input. The MB model with $C_{mean} = 1.42$ (green symbols) follows the experimental data closely over the entire Re range, with a maximum relative error of 5% (Fig. 2a). The gray band around it shows the effect of varying C between 1.37 and 1.47, indicating that the MB predictions are only weakly sensitive to the uncertainty in C and remain close to the measurements across the tested range. In contrast, the SB model (blue circles) overpredicts the pressure-loss coefficient, especially for Re above 2000 with relative errors of 10 to 55%. The EB model (red squares) underpredicts the pressure-loss coefficient as Re increases up to about 2300, and then overestimates the pressure-loss coefficient at higher Re above 3000, with errors spanning roughly -15 to +25%. Overall, the MB model provides the best agreement with the measured pressure-loss coefficients for the idealized stenosis model.

UIV-based trans-stenotic pressure gradient estimation

Figure 2b compares the measured pressure drop across the idealized stenosis model with predictions from the SB, EB, and MB models, where the black dashed $y = x$ line indicates perfect agreement. The yellow shaded band highlights the clinically relevant range in this model, corresponding to $Re \approx 2800 - 3900$ (i.e., $\Delta p = 10 - 15$ mmHg), where accurate pressure drop

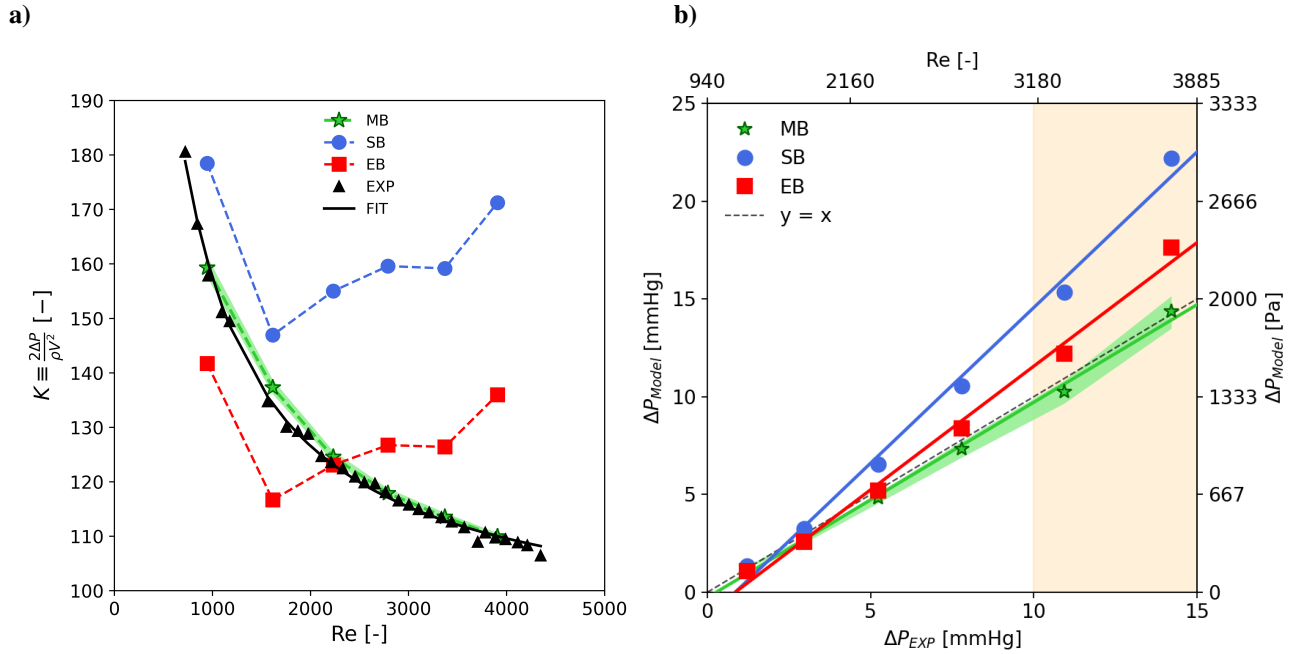


Figure 2. (a) Pressure-loss coefficient, K as function of Re . (b) Predicted pressure drop, ΔP_{Model} , versus measured trans-stenotic pressure drop, ΔP_{EXP} . MB (green; dashed) uses C_{mean} ; the grey band shows the range for $C = 1.37$ - 1.47 . SB = simplified Bernoulli; EB = extended Bernoulli; FIT = fitted correlation of experimental data (EXP). Pressure is reported in mmHg (bottom/left) and Pa. The dotted line in (b) is the identity line $y = x$. The yellow shaded band indicates clinically relevant Re number range for stenotic flows.

prediction is most important for clinical decision-making. Overall, the MB model with $C_{mean} = 1.42$ matches the measurements closely over the full range (1 – 15 mmHg) with an average error of 5% and a maximum error below 10%. The grey MB band obtained by varying C indicates that the predictions are weakly dependent on the uncertainty in C . In contrast, the SB model systematically overpredicts the pressure drop, with relative errors exceeding 50% and the bias increasing at higher values (up to about 22 mmHg predicted versus 14 mmHg measured). The EB model performs comparably to MB at low pressure drops, but starts overestimating for pressure gradients above 6 mmHg with relative errors spanning from about -15 to +25%, resulting in an intermediate performance between MB and SB at higher pressure gradients. In the clinically relevant regime, the MB model performs well with a maximum error below 5%. In contrast, the SB and EB models, overpredict the pressure drop with a maximum error of +55 and +25%, respectively.

These trends are confirmed by a statistical analysis, which is presented in Table 2. We have included an ordinary least-squares regression, root mean square error (RMSE), and the mean absolute percentage error, MAPE, for each model. The SB consistently overestimates the pressure drop, with a regression slope of 1.59 ($R^2 = 0.992$), large scatter (RMSE = 3.93 mmHg) and the highest relative error (MAPE = 29.9%). The EB also overpredicts, but more moderately (slope 1.26, $R^2 = 0.992$, RMSE = 1.51 mmHg, MAPE = 11.1%). As expected from the results in Fig. 2b, the MB approach using C_{mean} follows the agreement line (dashed black line) almost one-to-one (slope 0.998, $R^2 = 0.996$), with the smallest errors (RMSE = 0.404 mmHg, MAPE = 6.26%). Overall, the MB model with a Re -dependent loss coefficient presents the lowest errors within the considered regime.

| Method | MB at C_{mean} | SB | EB |
|------------------|------------------|-------|-------|
| Regression slope | 0.998 | 1.59 | 1.26 |
| R^2 | 0.996 | 0.992 | 0.992 |
| RMSE [mmHg] | 0.404 | 3.93 | 1.51 |
| MAPE % | 6.26 | 29.9 | 11.1 |

Table 2. Statistical comparison of model performance for predicting trans-stenotic pressure gradients in the idealized stenosis model. Shown are the regression slope against the line of identity, coefficient of determination (R^2), root mean square error (RMSE) and mean absolute percentage error (MAPE) for the MB, the SB, and the EB methods.

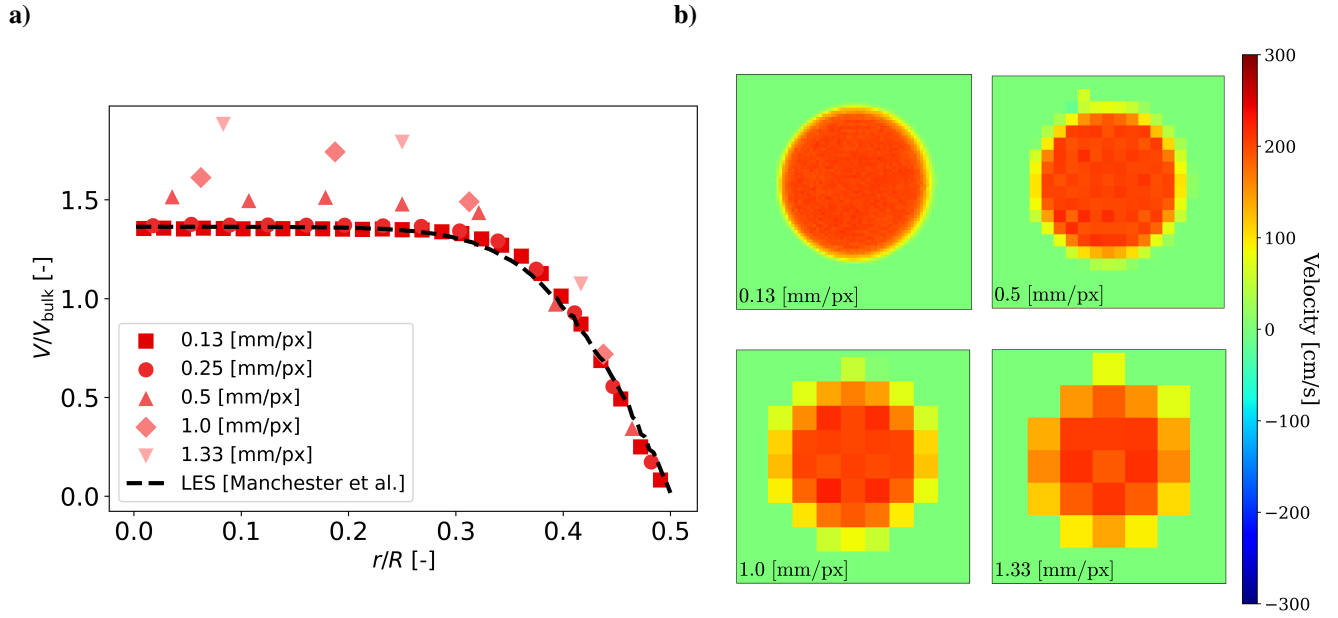


Figure 3. Effect of in-plane pixel size on the masked velocity profile at $z = -0.036$ m in the throat. (a) Normalized mean velocity profiles V/V_{bulk} from PC-MRI for five different pixel sizes 0.13 – 1.33 mm/px for $Re = 667$, compared with the reference profile at the same Re number⁴⁰. (b) Velocity maps at different pixel sizes, showing increasing PVE and a bias toward lower V_{bulk} as pixel size increases.

PC-MRI velocity fields

Figure 3b shows the normalized mean velocity profiles at $Re = 667$ for five different pixel sizes (0.13, 0.5, 1.0, and 1.33 mm/px) and a reference velocity profile obtained from large eddy simulation (LES)⁴⁰. For pixel sizes 0.13 and 0.25 mm/px, the lumen radius is sampled with 27 and 14 pixels, respectively, allowing the high-velocity core to be clearly resolved. At a pixel size of 0.50 mm/px, the lumen radius is sampled with 8 pixels, resulting in a more discretized velocity profile. This pixel density is still sufficient to capture the overall velocity profile. For the cases with a pixel size of 1.0 and 1.33 mm/px only 4 and 3 pixels represent the throat radius, respectively. This results in a velocity measurement that is dominated by partial volume effects (PVE), i.e., individual voxels contain a mixture of fast-moving fluid and slower moving flow, which smooths the velocity field and biases the voxel-averaged values⁴¹. Figure 3a illustrates representative PC-MRI velocity maps of the through-plane (axial) velocity component at the stenosis throat for four in-plane pixel sizes. It can be seen that the MRI data acquired with the smallest pixel size agrees well with the reference. However, increasing the pixel size leads to an underestimated mean velocity profile and smearing of the shear layer due to PVE.

Figure 4a summarizes the relative error in bulk velocity in the throat, computed by integrating the PC-MRI velocity over the segmented throat at $z = -0.036$ and comparing against the reference bulk velocity from the flowmeter. At 0.13 mm/px, the bulk velocity bias remains small (approximately -0.7 to -2.4% across the studied flow rates), increasing to roughly -1.7 to -8.5% at 0.25 mm/px. At 0.50 mm/px the underestimation becomes substantial (about -10 to -26%), and at 1.0 – 1.33 mm/px the bulk velocity is underestimated by approximately -27 to -45%, depending on the flow rate. Figure 4b summarizes the relative error in the peak throat velocity, computed by comparing the peak velocity at each pixel size against the corresponding peak velocity obtained at the smallest pixel size (0.13 mm/px). In contrast to the bulk velocity, the peak velocity shows a significantly weaker dependence on pixel size: at 0.25 and 0.50 mm/px the differences remain small (typically within about -0.6 to -2.1%), increasing to roughly -1.7 to -3.0% at 1.0 mm/px, and reaching approximately -5.0 to -6.1% at 1.33 mm/px, depending on the flow rate.

Figure 5 represents the relative errors in the mean throat velocity in terms of the number of pixels across the throat radius, N_{pixels} . Across all flow rates, reducing the pixel size to only 3 – 4 pixels across the throat radius (N_{pixels}) leads to substantial errors, with mean velocity underestimated by about -30 to -45%. As N_{pixels} increases, the error decreases monotonically. For $N_{\text{pixels}} \approx 13$, the velocity error falls below -10% for all flow rates. At the smallest pixel size with corresponding $N_{\text{pixels}} \approx 27$, the relative mean velocity error is reduced to a few percent only, ranging from -0.6 to -7%.

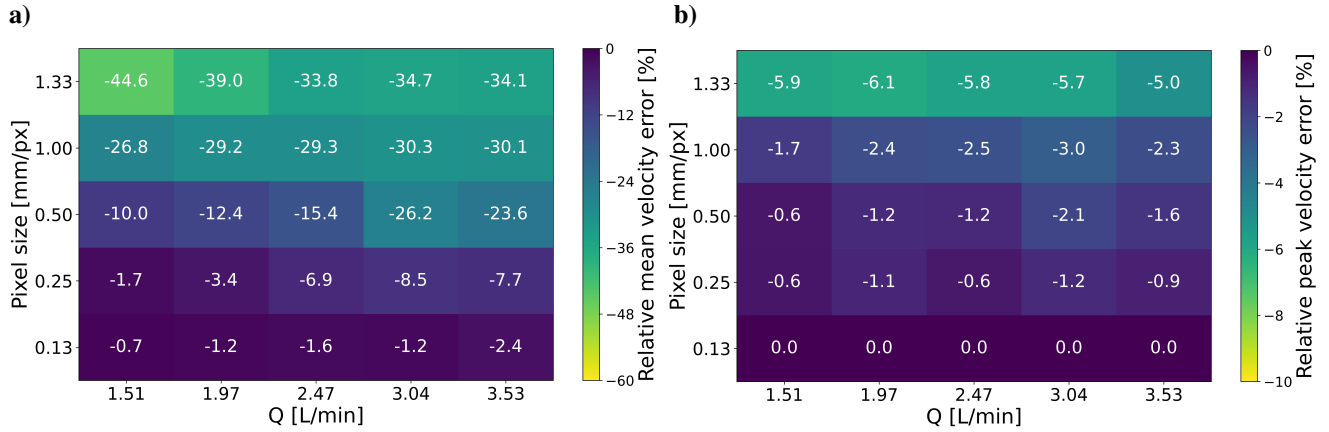


Figure 4. Heatmaps showing the effect of in-plane pixel size on MRI-based throat velocities in the idealized stenosis model. (a) Percentage error in mean throat velocity versus pixel size and flow rate Q , with respect to the reference; negative values indicate underestimation. (b) Percentage error in peak throat velocity versus pixel size and flow rate Q , computed relative to the peak velocity measured at the smallest pixel size (0.13 mm/px).

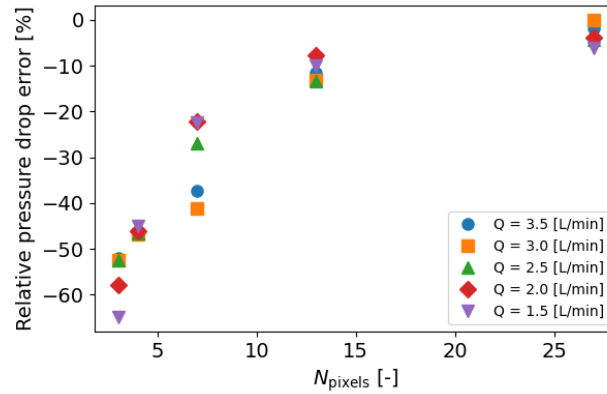


Figure 5. The effect of the in-plane pixel size on MRI-based mean velocity in the throat of the idealized stenosis model. Percentage error in mean throat velocity versus the number of pixels across the throat radius (N_{pixels}) for five steady flow rates ($Q = 1.5 - 3.5$ L/min) with respect to the reference flowrate measured by the flowmeter (negative indicates underestimation).

MRI-based trans-stenotic pressure gradient estimation

The flow-rates derived from the PC-MRI data were used to estimate the trans-stenotic pressure drop using the MB formulation (Eq. 8). These were compared against the measured pressure gradients. As shown in Fig. 6a, the relative pressure drop error closely mirrors the bulk-velocity error. As the pixel size increases, the MB-predicted pressure drop is increasingly underestimated, ranging from about -6% at 0.13 mm/px (approaching -2% at the highest flow rates) to approximately -22 to -41% at 0.50 mm/px. At 1.0 – 1.33 mm/px the underestimation reaches roughly -45 to -65%. This indicates that, once the MB loss correlation is defined by fitting to the experimental pressure-loss coefficients, the dominant limitation in MRI-based pressure estimation is the pixel-size-dependent bias in the measured throat velocities rather than the contribution of model itself. In Fig. 6b, the pressure drop is instead estimated using Eq. (9), based on the peak throat velocity and C_{mean} for all flow rates for the smallest pixel size (0.13 mm/px). In this case, the sensitivity to pixel size is markedly reduced: errors remain within approximately -3 to -13% across all flow rates, and increase only gradually toward the coarsest pixel sizes (up to about -18.7% at 1.33 mm/px).

Discussion

In this study, we examined how different flow regimes influence the pressure-loss coefficient K in an idealized stenosis model and introduced a Modified Bernoulli equation to predict the trans-stenotic pressure gradient. The accuracy and systematic

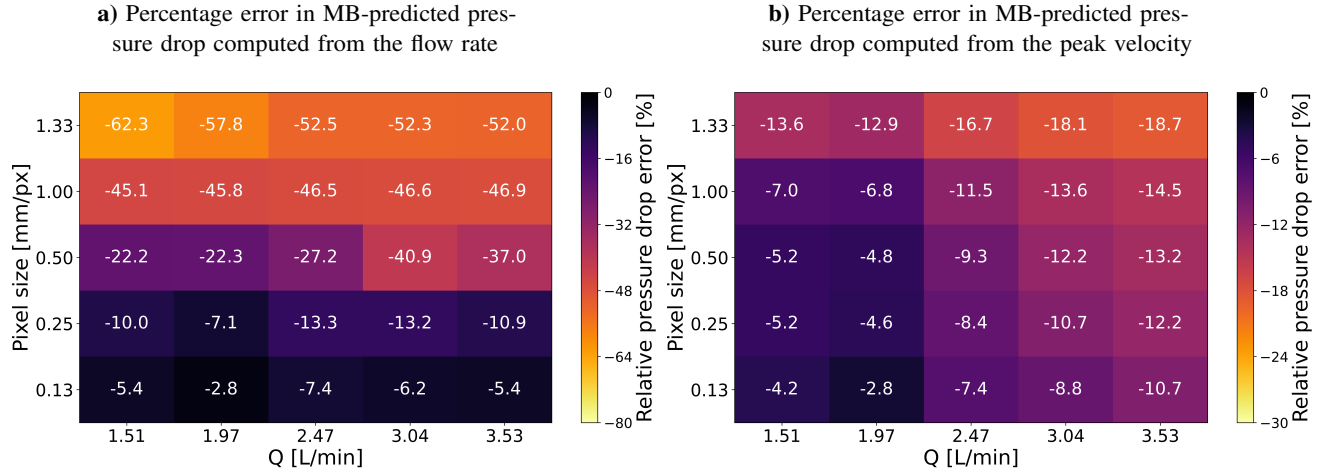


Figure 6. Heatmaps showing the effect of in-plane pixel size on MRI-based MB pressure drop estimates in the throat of the idealized stenosis model. (a) Percentage error in MB-predicted pressure drop computed from the flow-rate formulation (Eq. 8) versus pixel size and flow rate Q , with respect to the measured pressure drop data; negative values indicate underestimation. (b) Percentage error in MB-predicted pressure drop computed from the peak-velocity formulation (Eq. 9) using C_{mean} versus pixel size and flow rate Q , with respect to the measured pressure drop data.

biases of various Bernoulli-based models were investigated by comparing them with accurate experimental reference data. Additionally, we evaluated how MRI in-plane pixel size affects velocity accuracy and the resulting pressure drop estimates using the proposed modified Bernoulli model.

By incorporating flow physics into a pressure-loss coefficient formulation, we defined an MB model. The formulation of the MB model makes it flexible in terms of how it can be used in practice. Expressing the MB pressure gradient in terms of the throat peak velocity $V_{\text{peak,t}}$ makes it directly compatible with Doppler echocardiography, which measures this quantity routinely. On the other hand, rewriting the MB equation in terms of flow rate removes the need for direct peak velocity measurements and allows the trans-stenotic pressure gradient to be estimated from lumen area and flow, quantities that are accessible with PC-MRI or other imaging and flow-measurement techniques.

Comparing SB, EB, and MB across the tested flow regimes, we found that the MB model provided the closest agreement with the experimental data. Even when using a single averaged value for peak to bulk velocity ratio ($C_{\text{mean}} = 1.42$) rather than a case-specific ratio, the MB method kept errors within about $\pm 10\%$ across all flow conditions. In contrast, the SB model overestimated the pressure drop by up to 55%, with errors increasing at higher Re , consistent with previous observations^{6,15,42}. The EB model reduces this bias by accounting for the effective orifice area and associated pressure recovery, but still showed errors up to +25%, demonstrating that a pressure-recovery correction alone does not fully compensate for the flow physics.

The key point is that pressure loss is flow regime dependent²⁰, and the relevant regime in a stenosis is set by the throat Re number. In our approach, the throat Re number is rewritten as $Re_t = (D/D_t) \times Re$; for the present stenosis model $D/D_t = 3.03$, giving $Re_t \approx 3000 - 12000$, indicating that turbulent effects are important in stenotic flows^{32,40,43,44}. Consistent with this, 4D-flow MRI studies have linked turbulence production and turbulent kinetic energy dissipation to the trans-stenotic pressure drop^{6,22}. This explains why constant-coefficient SB and geometry-based EB formulations do not reliably capture losses as Re increases. Along similar lines, Oshinski et al.¹⁸ improved non-invasive gradients in aortic coarctation by using a stenosis-severity-dependent coefficient in $\Delta P = KV_{\text{peak,t}}^2$, but since K does not explicitly depend on the Re number, flow regime effects remain absorbed into a single empirical constant rather than as function of flow regime¹⁸. Therefore, it is important to take the flow regime into account when performing pressure measurements.

In our approach, the pressure-loss coefficient K is written as the sum of two contributions: a viscous term and a turbulent term. The fitted turbulent loss coefficient k_t for the trans-stenotic gradient was 1.41, in close agreement with the commonly used value of 1.52 reported by Seeley and Young³⁰. In contrast, for the viscous resistance coefficient k_v , Seeley and Young showed that there was a stronger geometrical dependence: in our case a value of $k_v = 62.4 \times 10^3$ was found, whereas they reported values spanning 421 to 56.2×10^3 (reported using the normalization $\Delta p/(\rho V^2)$; expressed in our normalization $2\Delta p/(\rho V^2)$ this corresponds to 842 to 112.4×10^3). This wide span supports the idea that in particular k_v is not a universal constant, but a parameter that should be reported and, when possible, tuned to a specific vessel or lesion. Recent work by Chernyavsky et al.⁴⁵ has shown that calibrating k_v and k_t to vessel elasticity and stenosis geometry substantially improves agreement between predicted and measured pressure-drops, which consolidates our current observations.

A critical component of the MB formulation is the velocity ratio $C = V_{\text{peak,t}}/V_{\text{bulk,t}}$, which bridges the gap between the peak velocities measured by clinical Doppler and the bulk flow rate. In our experiments, C varied between 1.37 and 1.47 across a wide range of measured flow rates. This variation reflects the flattening of the velocity profile for increasing Re . However, for a diagnostic tool to be clinically viable, it cannot require a complex, real-time measurement of the full velocity profile to determine the exact C for every stenosis geometry and flow rate. A recent study derived a similar flow-based expression for the SB equation by assuming a fixed velocity ratio $C = 1.5$ in cerebral venous flow and showed good agreement with CFD simulations³¹. This supports the practical idea of translating between flow rate and peak velocity via a prescribed C . Here we tested the validity of simplifying C to a single constant C_{mean} . Our results indicate that this simplification is remarkably robust. As shown by the narrow grey error bands in Fig. 2b, varying C across its entire observed range (1.37 – 1.47) resulted in only minor deviations in the predicted pressure drop. While the SB equation effectively ignores the shape of the velocity profile, the MB approach, even with a fixed C_{mean} , maintains its accuracy across all flow conditions.

Clinical guidelines grade native aortic stenosis (AS) by the mean transvalvular pressure drop: mild disease is characterized with mean gradients roughly below 20 – 25 mmHg, moderate 25 – 40 mmHg, and severe stenosis exhibits a gradient above 40 mmHg, where the exact boundaries depend also on the jet velocity and valve area⁴⁶. Since these thresholds directly determine follow-up and timing of valve intervention, errors in estimating the pressure drop - whether from ultrasound Doppler, MRI or analytical models - can reclassify a patient from mild to moderate or severe disease, leading to under- or overtreatment⁴⁶. The tested Re (1000 – 4000) in our experiments lie within the physiological band: recent in-vivo data from healthy subjects report mean Re numbers of about 1000 in the ascending aorta, with peak-systolic values between roughly 4000 and 9000 over the cardiac cycle; in the abdominal aorta and carotids, typical mean values are lower but can still reach several thousand during peak systole⁴⁷. In stenotic disease, Re can increase substantially with stenosis severity due to higher velocities in the stenosis area. In addition, as a result of activity or pharmacologic stress, the flow rate and thus Re in the stenosis will increase. As a consequence, the post-stenotic jet becomes more unstable, resulting in additional irreversible losses and thus a higher net pressure gradient. In our idealized stenosis model, the clinically relevant $\Delta p = 10 - 15 \text{ mmHg}$ band in Fig. 2b corresponds to pipe $Re \approx 2800 - 3900$. This range lies within the peak-systolic Re reported in vivo, highlighting that accurate pressure drop prediction in this band is important for assessing stenosis severity.

The MB model was calibrated from independent in-vitro pressure data as a Re -dependent loss coefficient and is formulated to be a function of either flow rate (Eq. 8) or peak throat velocity (Eq. 9). This structure makes the approach naturally compatible with PC-MRI, where the flow rate can be obtained by integrating the velocity field over a segmented lumen. However, the experiments also show that the benefit of a physics-based pressure model can be negated if the stenotic throat is not sufficiently resolved. Across the studied range, the throat bulk velocity is systematically underestimated as the in-plane pixel size increases. This is consistent with PVE due to the velocity near the wall and the relatively small number of pixels that span the cross-section. Because the pressure estimate from the MB model is directly affected by the measured mean velocities, this velocity bias propagates into a strong underestimation of the trans-stenotic pressure gradient for large pixel sizes. In other words, when the in-plane pixel size is small (e.g. 0.13 – 0.25 mm/px in our study), the MB model in combination with PC-MRI flow rates estimates the pressure drops within approximately 6 – 13% with respect to reference pressure drop measurements. When the pixel size is increased ($\geq 0.50 \text{ mm/px}$), the velocity underestimation dominates and the MB model underpredicts the pressure drop by 20 – 65%. To keep both quantities within a 10% error range, at least 15 – 20 pixels across the stenosis lumen are needed for the idealized stenotic model that we used for the current study. This corresponds to a pixel size in the order of one-tenth of the throat radius.

On the other hand, MB-predicted pressure drop using the peak velocity analysis adds an important point to this pixel size effect. While the mean throat velocity shows a strong negative bias with increasing pixel size, the peak throat velocity is robust, with deviations of only a few percent even at the coarsest sampling. As a result, when the MB pressure drop is computed from the peak velocity, the pressure errors are substantially lower and increase more gradually with pixel size (remaining within roughly -3 to -16% in our experiments). This contrast highlights that the large underestimation observed for the flow-rate-based formulation is primarily driven by the sensitivity of V_{bulk} to PVE and segmentation at the wall. In contrast, the peak-based formulation is less affected because V_{peak} is governed by the core of the lumen, and is less contaminated by PVE and averaging.

These findings provide an actionable guideline for protocol design: reliable MRI-based pressure estimation requires sufficient sampling across the stenosis lumen to limit partial-volume bias, particularly when the mean velocity used in the MB formulation. While the exact threshold will depend on the signal-to-noise ratio, segmentation strategy, slice thickness, and stenosis geometry, the combined heatmaps provide a concrete pixel-size–error map for both bulk- and peak-based MB implementations in this idealized stenosis model. This map can be used to balance scan time with the accuracy required to obtain clinically meaningful and accurate pressure gradients.

In this study we used the FDA benchmark nozzle in combination with water as a working fluid to represent an idealized stenotic model. In contrast, physiological stenoses are more complex in geometry (asymmetry, eccentricity, curvature) and blood exhibits non-Newtonian rheology, especially at lower shear rates. The translation to *in vivo* conditions needs further

investigation. Even though the empirical MB correlation introduced in this study was specifically calibrated for the FDA nozzle, the underlying workflow provides a template for clinical application. The parameters are not arbitrary fit constants; they are deterministic functions of stenosis geometry, including the contraction ratio, lesion length, eccentricity, and entrance angles.

In future work, one could build a “library” of (k_v , k_t , C_{mean}) values for a set of representative anatomical profiles. This would allow for the selection of appropriate k_v , k_t , and C_{mean} from this pre-calibrated library based on the stenosis morphology seen on medical imaging without the need to re-derive these parameters for each patient, retaining the accuracy of the MB formulation without requiring invasive calibration in every individual case.

A second limitation of this study relates to the inflow condition. Although our experiments used a steady inflow, this was a reasonable surrogate for peak-systolic conditions. A study was done by Young and Tsai²⁸ to see how the unsteadiness affects the pressure drop. Young et al. extended their steady stenosis model to harmonically oscillating flow by adding an inertial term. The unsteady pressure gradient was written as a sum of a viscous term with coefficient k_v , a turbulence term with coefficient k_t (same form as in steady flow), and an inertial term proportional to dV/dt with coefficient k_i . Using the steady flow values of k_v and k_t together with $k_i \approx 1$, they could predict the peak pressure drop in pulsatile experiments with an error less than 20%. For severe stenoses, viscous and turbulence effects dominated the pressure loss mechanism, so the behavior was close to quasi-steady. Therefore, the pressure-loss peak occurred almost at the same time as the flow rate peak, and the peak value was only slightly smaller than the steady flow prediction. Overall, they concluded that for severe stenoses the peak pressure gradient in pulsatile flow is well described by steady flow loss coefficients with a small inertial correction, supporting the common quasi-steady interpretation of peak-systolic gradients. Therefore, based on these results we deemed it justified to ignore pulsatile effects in our current model.

Another limitation of our work is the rigid nature of the FDA nozzle and piping, whereas real arteries are elastic. Chernyavsky et al.⁴⁵ showed that in coronary stenoses, vessel compliance can modify the pressure drop by an amount comparable to viscous effects, and that accounting for compliance improves the prediction of fractional flow reserve (FFR), defined as the ratio of distal to proximal pressure across a stenosis under hyperaemia. In our study, the calibrated coefficients therefore represent a rigid-wall limit; future extensions of the MB framework should account for arterial elasticity via modified loss coefficients before being applied to highly compliant vascular beds. Incorporating pulsatility, Re -dependent correlations, and wall compliance will be important to assess the robustness of these findings under physiological conditions.

To conclude, we developed and calibrated a Re -dependent MB model using experimentally measured pressure drops and high-resolution velocity data obtained with ultrasound Doppler and MRI. Compared with SB and EB, the MB model provided the closest agreement with the experimental pressure gradients across the tested conditions and in the clinically relevant Re number range. We further showed that MRI-based pressure estimates are primarily limited by pixel-size-dependent bias in throat velocities. Increasing the in-plane pixel size leads to systematic underestimation of both velocity and pressure drop, whereas sufficiently small in-plane pixel sizes keep MB pressure errors on the order of 10%. Notably, the peak throat velocity was substantially less sensitive to pixel size than bulk velocity, which reduced the pressure drop error when the MB formulation was expressed in terms of $V_{\text{peak,t}}$ (with a constant C_{mean}). Together, these results address the two main gaps highlighted in the introduction by incorporating regime-dependent losses through an explicit Re dependence and quantifying how MRI in-plane pixel size impacts trans-stenotic pressure gradient estimations.

Data availability

The dataset generated during and/or analyzed during the current study is available from the corresponding author on request.

References

1. Thiriet, M., Delfour, M. & Garon, A. Vascular stenosis: An introduction. In Lanzer, P. (ed.) *PanVascular Medicine*, DOI: https://doi.org/10.1007/978-3-642-37078-6_32 (Springer, Berlin, Heidelberg, 2015).
2. Lindman, B. R. *et al.* Calcific aortic stenosis. *Nat. Rev. Dis. Primers* **2**, 16006, DOI: <https://doi.org/10.1038/nrdp.2016.6> (2016).
3. Messas, E. *et al.* Management of carotid stenosis for primary and secondary prevention of stroke: state-of-the-art 2020: a critical review. *Eur. Hear. J. Suppl.* **22**, M35–M42, DOI: <https://doi.org/10.1093/eurheartj/suaa162> (2020).
4. Ross, R. & Glomset, J. A. The pathogenesis of atherosclerosis (first of two parts). *New Engl. J. Medicine* **295**, 369–377, DOI: <https://doi.org/10.1056/NEJM197608122950707> (1976).
5. Paraskevas, K. I. *et al.* Recent advances and controversial issues in the optimal management of asymptomatic carotid stenosis. *J. Vasc. Surg.* **79**, 695–703, DOI: <https://doi.org/10.1016/j.jvs.2023.11.004> (2024).
6. Ha, H., Lantz, J., Ziegler, M. *et al.* Estimating the irreversible pressure drop across a stenosis by quantifying turbulence production using 4d flow MRI. *Sci. Reports* **7**, 46618, DOI: <https://doi.org/10.1038/srep46618> (2017).

7. Zardkoohi, O. & Grimm, R. A. Echocardiography. In Askari, A. T. & Messerli, A. W. (eds.) *Cardiovascular Hemodynamics: An Introductory Guide*, 155–181, DOI: https://doi.org/10.1007/978-1-60761-195-0_6 (Springer International Publishing, Cham, 2019).
8. Markl, M., Frydrychowicz, A., Kozerke, S., Hope, M. D. & Wieben, O. 4d flow MRI. *J. Magn. Reson. Imaging* **36**, 1015–1036, DOI: <https://doi.org/10.1002/jmri.23632> (2012).
9. Soulat, G., McCarthy, P. & Markl, M. 4d flow with MRI. *Annu. Rev. Biomed. Eng.* **22**, 103–126, DOI: <https://doi.org/10.1146/annurev-bioeng-100219-110055> (2020).
10. Allen, B. D., Burris, N. S., Lombardi, P. J. & Francois, C. J. Four-dimensional flow magnetic resonance imaging in cardiothoracic imaging. *Adv. Clin. Radiol.* **1**, 43–54, DOI: <https://doi.org/10.1016/j.yacr.2019.04.002> (2019).
11. Dirix, P., Buoso, S., Peper, E. S. & Kozerke, S. Synthesis of patient-specific multipoint 4d flow MRI data of turbulent aortic flow downstream of stenotic valves. *Sci. Reports* **12**, 16004, DOI: <https://doi.org/10.1038/s41598-022-20121-x> (2022).
12. Cherry, M., Khatir, Z., Khan, A. *et al.* The impact of 4d-flow MRI spatial resolution on patient-specific CFD simulations of the thoracic aorta. *Sci. Reports* **12**, 15128, DOI: <https://doi.org/10.1038/s41598-022-19347-6> (2022).
13. Anavekar, N. S. & Oh, J. K. Doppler echocardiography: a contemporary review. *J. Cardiol.* **54**, 347–358, DOI: <https://doi.org/10.1016/j.jjcc.2009.10.001> (2009).
14. Gill, H. *et al.* Evaluation of aortic stenosis: From Bernoulli and Doppler to Navier–Stokes. *Trends Cardiovasc. Medicine* **33**, 32–43, DOI: <https://doi.org/10.1016/j.tcm.2021.12.003> (2023).
15. Kazemi, A., Padgett, D. A., Callahan, S., Stoddard, M. & Amini, A. A. Relative pressure estimation from 4d flow mri using generalized bernoulli equation in a phantom model of arterial stenosis. *Magn. Reson. Mater. Physics, Biol. Medicine* **35**, 733–748, DOI: <https://doi.org/10.1007/s10334-022-01001-x> (2022).
16. Paraskevas, K. I. *et al.* Recent advances and controversial issues in the optimal management of asymptomatic carotid stenosis. *J. Vasc. Surg.* **79**, 695–703, DOI: <https://doi.org/10.1016/j.jvs.2023.11.004> (2024).
17. Sakthi, C., Yee, H. & Kotlewski, A. Overestimation of aortic valve gradient measured by doppler echocardiography in patients with aortic stenosis. *Catheter. Cardiovasc. Interv.* **65**, 176–179, DOI: <https://doi.org/10.1002/ccd.20324> (2005).
18. Oshinski, J. N. *et al.* Improved measurement of pressure gradients in aortic coarctation by magnetic resonance imaging. *J. Am. Coll. Cardiol.* **28**, 1818–1826, DOI: [https://doi.org/10.1016/S0735-1097\(96\)00395-6](https://doi.org/10.1016/S0735-1097(96)00395-6) (1996).
19. Garcia, D., Pibarot, P., Dumesnil, J. G., Sakr, F. & Durand, L. G. Assessment of aortic valve stenosis severity: a new index based on the energy loss concept. *Circulation* **101**, 765–771, DOI: <https://doi.org/10.1161/01.CIR.101.7.765> (2000).
20. White, F. M. *Fluid Mechanics* (McGraw-Hill, 2011), 7 edn.
21. Casas, B., Lantz, J., Dyverfeldt, P. & Ebbers, T. 4d flow MRI-based pressure loss estimation in stenotic flows: Evaluation using numerical simulations. *Magn. Reson. Medicine* **75**, 1808–1821, DOI: <https://doi.org/10.1002/mrm.25772> (2016).
22. Dyverfeldt, P., Hope, M. D., Tseng, E. E. & Saloner, D. Magnetic resonance measurement of turbulent kinetic energy for the estimation of irreversible pressure loss in aortic stenosis. *JACC: Cardiovasc. Imaging* **6**, 64–71, DOI: <https://doi.org/10.1016/j.jcmg.2012.07.017> (2013).
23. Maréchaux, S. *et al.* Usefulness of exercise-stress echocardiography for risk stratification of true asymptomatic patients with aortic valve stenosis. *Eur. Hear. J.* **31**, 1390–1397, DOI: <https://doi.org/10.1093/eurheartj/ehq076> (2010).
24. Otto, C. M. *et al.* Physiologic changes with maximal exercise in asymptomatic valvular aortic stenosis assessed by Doppler echocardiography. *J. Am. Coll. Cardiol.* **20**, 1160–1167, DOI: [https://doi.org/10.1016/0735-1097\(92\)90373-U](https://doi.org/10.1016/0735-1097(92)90373-U) (1992).
25. Gorlin, R., Sawyer, C. G., Haynes, F. W., Goodale, W. T. & Dexter, L. Effects of exercise on circulatory dynamics in mitral stenosis. III. *Am. Hear. J.* **41**, 192–203, DOI: [https://doi.org/10.1016/0002-8703\(51\)90099-3](https://doi.org/10.1016/0002-8703(51)90099-3) (1951).
26. Young, D. F. & Tsai, F. Y. Flow characteristics in models of arterial stenoses. i. steady flow. *J. Biomech.* **6**, 395–410, DOI: [https://doi.org/10.1016/0021-9290\(73\)90099-7](https://doi.org/10.1016/0021-9290(73)90099-7) (1973).
27. Morgan, B. E. & Young, D. F. An integral method for the analysis of flow in arterial stenoses. *Bull. Math. Biol.* **36**, 39–53, DOI: [https://doi.org/10.1016/S0092-8240\(74\)80005-4](https://doi.org/10.1016/S0092-8240(74)80005-4) (1974).
28. Young, D. F. & Tsai, F. Y. Flow characteristics in models of arterial stenoses — ii. unsteady flow. *J. Biomech.* **6**, 547–559, DOI: [https://doi.org/10.1016/0021-9290\(73\)90012-2](https://doi.org/10.1016/0021-9290(73)90012-2) (1973).
29. Padmanabhan, N. Mathematical model of arterial stenosis. *Med. Biol. Eng. Comput.* **18**, 281–286, DOI: <https://doi.org/10.1007/BF02443380> (1980).

30. Seeley, B. D. & Young, D. F. Effect of geometry on pressure losses across models of arterial stenoses. *J. Biomech.* **9**, 439–448, DOI: [https://doi.org/10.1016/0021-9290\(76\)90086-5](https://doi.org/10.1016/0021-9290(76)90086-5) (1976).
31. Sidora, G., Haley, A. L., Cancelliere, N. M., Pereira, V. M. & Steinman, D. A. Back to bernoulli: a simple formula for trans-stenotic pressure gradients and retrospective estimation of flow rates in cerebral venous disease. *J. NeuroInterventional Surg.* **17**, 1005–1010, DOI: <https://doi.org/10.1136/jnis-2024-022074> (2025).
32. Hariharan, P. *et al.* Multilaboratory particle image velocimetry analysis of the fda benchmark nozzle model to support validation of computational fluid dynamics simulations. *J. Biomech. Eng.* **133**, 041002, DOI: <https://doi.org/10.1115/1.4003440> (2011).
33. Ono, K. A comprehensive report on ultrasonic attenuation of engineering materials, including metals, ceramics, polymers, fiber-reinforced composites, wood, and rocks. *Appl. Sci.* **10**, 2230, DOI: <https://doi.org/10.3390/app10072230> (2020).
34. Gurung, A. & Poelma, C. Measurement of turbulence statistics in single-phase and two-phase flows using ultrasound imaging velocimetry. *Exp. Fluids* **57**, 171, DOI: <https://doi.org/10.1007/s00348-016-2266-x> (2016).
35. Poelma, C. Ultrasound imaging velocimetry: a review. *Exp. Fluids* **58**, 3, DOI: <https://doi.org/10.1007/s00348-016-2283-9> (2017).
36. Westerweel, J. *Digital particle image velocimetry: Theory and application*. Ph.D. thesis, Delft University of Technology (1993). PhD thesis.
37. Westerweel, J., Dabiri, D. & Gharib, M. The effect of a discrete window offset on the accuracy of cross-correlation analysis of digital PIV recordings. *Exp. Fluids* **23**, 20–28, DOI: <https://doi.org/10.1007/s003480050082> (1997).
38. Scarano, F. Iterative image deformation methods in PIV. *Meas. Sci. Technol.* **13**, R1, DOI: <https://doi.org/10.1088/0957-0233/13/1/201> (2001).
39. Bernstein, M. A., King, K. F. & Zhou, X. J. *Handbook of MRI Pulse Sequences: A Guide for Scientists, Engineers, Radiologists, and Technologists* (Elsevier Academic Press, 2004).
40. Manchester, E. L. & Xu, X. Y. The effect of turbulence on transitional flow in the FDA’s benchmark nozzle model using large-eddy simulation. *Int. J. for Numer. Methods Biomed. Eng.* **36**, DOI: <https://doi.org/10.1002/cnm.3389> (2020).
41. Hamilton, C. A. Correction of partial volume inaccuracies in quantitative phase contrast MR angiography. *Magn. Reson. Imaging* **12**, 1127–1130, DOI: [https://doi.org/10.1016/0730-725X\(94\)91245-R](https://doi.org/10.1016/0730-725X(94)91245-R) (1994).
42. Falahatpisheh, A. *et al.* Simplified Bernoulli’s method significantly underestimates pulmonary transvalvular pressure drop. *J. Magn. Reson. Imaging* **43**, 1313–1319, DOI: <https://doi.org/10.1002/jmri.25097> (2015).
43. Ahmed, S. A. & Giddens, D. P. Pulsatile poststenotic flow studies with laser doppler anemometry. *J. Biomech.* **17**, 695–705, DOI: [https://doi.org/10.1016/0021-9290\(84\)90123-4](https://doi.org/10.1016/0021-9290(84)90123-4) (1984).
44. Varghese, S. S., Frankel, S. H. & Fischer, P. F. Direct numerical simulation of stenotic flows. part 1. steady flow. *J. Fluid Mech.* **582**, 253–280, DOI: <https://doi.org/10.1017/S0022112007005848> (2007).
45. Chernyavsky, B., Mouzali, N., Glanz, V. & Velikorodny, A. Investigation of the pressure drop in arterial models with stenoses using numerical and experimental in vitro approaches: effect of elasticity. *Int. J. for Numer. Methods Biomed. Eng.* **41**, e70099, DOI: <https://doi.org/10.1002/cnm.70099> (2025).
46. Baumgartner, H. *et al.* Recommendations on the echocardiographic assessment of aortic valve stenosis: a focused update from the european association of cardiovascular imaging and the american society of echocardiography. *Eur. Hear. J. – Cardiovasc. Imaging* **18**, 254–275, DOI: <https://doi.org/10.1093/ehjci/jew335> (2017).
47. Menon, K., Hu, Z. & Marsden, A. L. Cardiovascular fluid dynamics: a journey through our circulation. *Flow* **4**, E7, DOI: <https://doi.org/10.1017/flo.2024.5> (2024).

Acknowledgements

We acknowledge Prof. Christian Poelma for valuable discussions on the UIV data analysis and for providing access to the UIV measurement facilities. This project was supported by TU Delft faculty of Mechanical Engineering through a ME Cohesion grant awarded to S.P. and W.H.

Author contributions statement

A.A.: Conceptualization, Data curation, Formal analysis, Investigation, Methodology, Project administration, Resources, Software, Validation, Visualization, Writing – original draft, Writing – review & editing. J.T.P.: Conceptualization, Methodology, Project administration, Supervision, Writing – review & editing. S.P.: Conceptualization, Funding acquisition, Methodology, Project administration, Resources, Supervision, Visualization, Writing – review & editing. W.H.: Conceptualization, Funding acquisition, Methodology, Project administration, Resources, Software, Supervision, Validation, Visualization, Writing – review & editing.

Competing interests

The authors declare no competing interests.

Additional information

Supplementary Information The online version contains supplementary material.

Correspondence and requests for materials should be addressed to S.P. and W.H.